Displacement of extracellular chloride by sulfated glycosaminoglycans of the brain's extracellular matrix

Abstract

GABA is the primary inhibitory neurotransmitter. Membrane currents evoked by $GABA_A$ receptor activation have uniquely small driving forces: their reversal potential (E_{GABA}) is very close to the resting membrane potential. As a consequence, $GABA_A$ currents can flow in either direction, depending on both the membrane potential and the local intra and extracellular concentrations of the primary permeant ion, chloride (Cl). Cytoplasmic Cl concentrations vary widely due to displacement of mobile Cl ions by relatively immobile anions. Here we describe new reporters of extracellular chloride (Cl^-_o) and demonstrate that Cl is displaced in the extracellular space by high and spatially heterogenous concentrations of sulfated glycosaminoglycans. The mean Cl^-_o is only half the canonical concentration, i.e. the Cl concentration in the cerebrospinal fluid. Cl^-_o microdomains provide a mechanism to link the highly stable distribution of GAGs in the brain's extracellular space to neuronal signal processing via the effects on the amplitude and direction of $GABA_A$ transmembrane Cl currents.

Introduction

$GABA_A$ synapses comprise the primary output for inhibitory interneurons in the brain (Hu et al. 2014; Tremblay et al. 2016). A unique feature of $GABA_A$ synapses are the very small driving forces for ion flux through open $GABA_A$ receptor-operated membrane channels. The reversal potential for the primary permeant ion, chloride, is usually within a few mV of the neuronal resting membrane potential (RMP; Thompson et al. 1988), and may even be positive to RMP (Staley and Mody 1992; Tyzio et al. 2008). This low driving force makes possible a novel form of synaptic plasticity at $GABA_A$ synapses: the direction of current flow, i.e. the effect of $GABA_A$ receptor activation on membrane potential, can be reversed by low millimolar alterations in the local chloride concentration (Coombs et al. 1955). Such physiological variance is routinely observed in individual studies (e.g. Ebahara et al. 1995; Huberfeld et al. 2007) and is likely to underlie the 25 mV range of reported group mean reversal potentials in 20 recent studies of evoked $GABA_A$ currents recorded with gramicidin perforated patch electrodes in area CA1 of the hippocampus (tabulated in Rahtmati et al. 2021). This variance has substantial effects on synaptic signaling: the $GABA_A$ currents evoked in a single pyramidal cell by stimulation of 8 different presynaptic interneurons also varied by over 20 mV (Rahmati et al. 2021).

We have proposed that the intracellular chloride concentration (Cl^-_i) is not monotonic across the neuronal cytoplasm, but rather varies inversely with the local concentration of macromolecular anions that comprise the vast majority of intracellular anions (Glykys et al. 2014; Rahmati et al. 2021). This phenomenon is known as Donnan exclusion (Epsztein et al. 2018; Gao et al. 2022). Mobile ions, in this case Cl, are repelled by relatively immobile ions such as proteins with negative surface charges. Many proteins such as gephryn that are associated with $GABA_A$ synapses bear large negative surface charges (Sola et al, 2001), suggesting that variance in the $GABA_A$ reversal potential (E_{GABA}) is determined by local fixed charge densities. However, E_{GABA} is determined not only by Cl^-_i but rather by the ratio of intra vs extracellular permeant ions. This raises the possibility that spatial variance in the extracellular Cl concentration (Cl^-_o) could also be an important determinant of E_{GABA}.

The displacement of Cl^- by fixed negative charges should also occur in the extracellular space, where the high negative charge density of the polysulfated glycosaminoglycans (GAGs) that comprise the bulk of the extracellular matrix can be as high as the Cl^- concentration in the CSF (Urban et al. 1979; Chahine et al. 2005; Morwaski et al. 2015). Thus some to all of the local Cl^-_o could be displaced, depending on the degree of GAG sulfation. Such displacement has been most clearly demonstrated in the matrix of cartilaginous tissue, where the negative charge density of the extracellular matrix can reach 400 meq / liter (Lesperance et al. 1992), but dozens of mM of Cl^-_o are also displaced by sulfated GAGs in tissues such as skin (Titze et al. 2004).

Many findings suggest that the brain Cl^-_o is lower than the cannoncal value. Xray emission spectroscopy of the extracellular space has demonstrated sulfate concentrations as high as 100 mM (Morawski et al. 2015). Astrocytic buffering of Cl^-_o (Egawa et al. 2013) would be of little utility if Cl^-_o were > 100 mM. The gating of Group II and III metabotropic glutamate receptors, kainate receptors, acid-sensing membrane ion channels, and the transport rate of the GlyT1 glycine transporter, are strongly modulated by Cl^-_o over the range of 1 - 100 mM (Kuang et al. 2006; Plested et al. 2007; Kusama et al. 2010; DiRaddo et al. 2015; Tora et al. 2018; Zhang et al. 2021). Such strong modulation by low Cl^-_o would not make sense if Cl^-_o was uniformly > 100 mM.

Studies of Cl^-_o are few, and have only been carried out with relatively large multibarreled ion-sensitive electrodes with tip diameters of 3-5 um (Jiang et al. 1992). This technique creates a stab wound in the tissue that is surrounded by bulk extracellular fluid (containing no GAGs), that will have a Cl^- concentration that is close to that of the perfusate. Modern Cl-selective microelectrodes are less damaging, and those studies demonstrate variance in Cl^-_o, but of only a few mM (Kroeger et al. 2010).

A fluorometric study of Cl^-_o would be the ideal means to establish the distribution of chloride in the extracellular space. However, no suitable Cl-sensitive organic fluorophores exist, and transgenic fluorophores such as SuperClomeleon (Grimley et al. 2013) and CloPhensor (Sulis Sato et al. 2017) are not distributed in the extracellular space. We therefore developed a chloride-sensitive fluorophore from previously described organic backbones (Biwersi et al. 1992) that satisfied the following criteria. First, the fluorophore needs to be sensitive to Cl in the range of the extracellular chloride concentration i.e. ~ 100 mM; available fluorophores have been optimized for the low millimolar chloride concentrations of the cytoplasm. Second, the fluorophore needs to report Cl independently of the concentration of fluorophore. Ratiometric fluorophores suitable for the extracellular space do not exist, so we used Fluorescence Lifetime Imaging (FLIM; Kaneko et al. 2004) to remove the dependence of the fluorescence emission on fluorophore concentration. Third, the fluorophore needs to be constrained to the extracellular space, for which dextran conjugation is optimal (Xiao et al. 2008; Tonneson et al. 2018). Fourth, the fluorophore needs to be excited by wavelengths that are not damaging to brain tissue, i.e. below the ultraviolet range and in the visible or infrared range. Fifth, many Cl sensors are also sensitive to pH (Kuner and Augustine 2000; Grimley et al. 2013), so a pH-insensitive fluorophore would be ideal. Finally, the fluorophore needs to be sufficiently bright so that its emission can be reliably distinguished from autofluorescence.

Here, we describe: a newly synthesized Cl-sensitive fluorophore that meets these 6 criteria; the demonstration of stable Donnan exclusion of chloride by sulfates fixed to GAG-like carbohydrate polymers; the demonstration that the Cl^-_o of in vitro and in vivo brain tissue is much lower than cerebrospinal or plasma chloride; a remarkable spatial variance in Cl^-_o (i.e. Cl^-_o microdomains); finally, as evidence that Cl^-_o is determined by Donnan exclusion of Cl by sulfated GAGs, we demonstrate that release of these sulfates by exogenous chondroitinase results in an increase in Cl^-_o.

Methods

General: Chemicals were purchased from Sigma-Aldrich (St Louis, MO) unless otherwise noted. Solutions are brought up in distilled water unless otherwise noted. Standard aCSF was brought up in 18MΩ water and consisted of (in mM): NaCl 126; KCl 3.5; $CaCl_2$ 2; $MgCl_2$ 1.3; NaH_2PO4 1.2; Glucose 11; $NaHCO_3$ 15. Low chloride aCSF variant was identical except that sodium gluconate was substituted for NaCl, resulting in 10mM Cl^-. Calibration solutions were made by mixing appropriate proportions of standard aCSF with low chloride aCSF such that a chloride and gluconate sum total of 136mM was maintained while Cl^- ranged from 10 to 136mM. Colorimetric assays were read using a Wallac Victor-2 1420 spectrophotometer with a halogen continuous wave light source and spectral line filters at listed wavelength +/- 5 to 10nm. Centrifugation steps were accomplished in a tabletop Eppendorf 5417R microcentrifuge. Reflux apparatus for synthesis consisted of a recirculating cooling bath (Fisher Scientific) filled with ethylene glycol cooling a 24/40 double-lumen coiled reflux tube (Ace Glassware, Vineland, NJ)

with a 500mL round bottom flask (Corning) heated with a heating mantle regulated by a timed power controller (Glas-Col #O406 and #104A PL312, respectively).

Synthesis of ABP-dextran: The process of optimizing a bright, redshifted, pH-insensitive fluorophore that is responsive to chloride concentration over a dynamic range inclusive of expected extracellular chloride concentrations is beyond the scope of this paper and will be published separately (manuscript in preparation). Synthesis techniques closely followed those of the Verkman group when synthesizing related compounds (Verkman, 1990; Biwersi et al., 1992) and conjugating to dextran (Biwersi et al., 1992). Briefly, N(4-***a***mino***b***utyl)***p***henantridinium (ABP) was synthesized by a reflux of equimolar amounts of phenanthridine and N(4-bromobutyl)phthalimide in acetonitrile followed by a second reflux in 6N HCl to hydrolyze phthalate. Product was twice recrystallized from 95% ethanol before conjugation to cyanogen bromide-activated 10,000g/moL (10KDa) dextran, producing 10KDa ABP-dextran with an approximate labeling ratio of 12.

Sulfation of agarose: We modified the method of Fuse and Suzuki (Fuse and Suzuki, 1975) to add sulfate groups to the repeating disaccharide units of agarose; full details are supplied as a supplement. Briefly, agarose was dissolved in DMSO at 4% (w/v) at room temperature before being cooled to 4C and stirred with 0.4 volumes pre-chilled 4:1 acetic anhydride / glacial acetic acid for 15 minutes. Sulfuric acid (15.6M) is then added slowly at a 6:1 molar ratio to agarose repeating disaccharide units. Mixture is then moved to ambient temperature and allowed to stir for 15 minutes before reaction is stopped by neutralization with 10M NaOH. Sulfated agarose is then dialyzed at ambient temperature in 12-14KDa dialysis tubing (SpectraPor) against 15 volumes of 50mM Tris pH 7.4 once, then against distilled water changed twice daily until dialysate clarifies. Agarose is then precipitated in 95% ethanol, vacuum filtered, and oven-dried. Material is stored at ambient temperature in sealed glass vial until use.

Measurement of [SO42-] in agar or agarose: $BaCl_2$-gelatin turbidimetric method (Torres et al., 2021) was used to quantify sulfate content of gel materials. Sulfated agarose product or commercially available agarose or agar powder was dissolved in 0.5M HCl at a concentration of 5% (w/v) in 2mL screw-top microtubes with gasket (Fisher Scientific). Tubes are then placed in a heat block at 100-110C for 3hours with periodic vortex mixing, hydrolyzing the sugar backbone and releasing sulfate. All samples had varying amounts of insoluble dark brown precipitated sugar, which was clarified at 20,000 x g for 10 minutes. Standards are diluted from 1M Na_2SO_4 stock in 0.5M HCl. $BaCl_2$-gelatin reagent is freshly prepared by dissolving 30mg gelatin in 10mL distilled water at 80C for 10minutes, then promptly adding 100mg $BaCl_2$ and vortex mixing. $BaCl_2$-gelatin is then allowed to cool passively before use. Samples are prepared by combining 1 part sample (diluted as desired), 1 part $BaCl_2$-gelatin, and 3 parts 0.5M HCl. Assay is performed in a glass-bottom 96-well plate reading absorbance at 405nm. Multiple sample dilutions were prepared and concentrations were calculated only from dilutions whose readings were well within the dynamic range of the standards.

Measurement of Cl^- in agar or agarose gels (chemical method): Chloride was measured colorimetrically using mercury(II) thiocyanate ($Hg(SCN)_2$) / iron(III) nitrate ($Fe(HNO_3)_3$) absorbance method of Florence and Farrar (Florence and Farrar, 1971) to infer Cl^- from $Fe(SCN)_3$ production through the two-step reaction,

$$[\mathrm{Hg(SCN)_2} + 2\mathrm{Cl^-} \rightleftharpoons \mathrm{HgCl_2} + 2\mathrm{SCN^-}]\mathrm{x}3$$

$$[3SCN^- + Fe(NO_3)_3 \rightleftharpoons Fe(SCN)_3 + 3(NO_3)^-]x2$$

reading $Fe(SCN)_3$ absorbance at 490nm. Briefly, agar or agarose gels cast at 5% (w/v) in 3.5cm Petri dishes were drained by gravity and then Kimwipes were used to gently wick away remaining excess fluid at sides of dish. Similar amounts of each sample are transferred to 2mL screw-top microtubes with gasket (Fisher Scientific) and 1 gel volume, estimated by weight, of 7.8M nitric acid (HNO_3) is added (final [HNO_3] = 3.9M). Samples are then placed in a heat block at 100-110C for 3hours with periodic vortex mixing, hydrolyzing the sugar backbone to break down the gel lattice. All samples had varying amounts of insoluble dark brown precipitated sugar, which was clarified at 20,000 x g for 10 minutes. A portion of supernatant or KCl standard, diluted with 0.3M HNO_3, was combined with one-tenth volumes of 0.4M $Fe(NO_3)_3$ (in 4M nitric acid) and saturated $Hg(SCN)_2$ (in ethanol), triturated, and allowed 20minutes for reaction to reach endpoint. Stock solutions are used within 1week. Multiple sample dilutions were prepared and concentrations were calculated only from dilutions whose readings were well within the dynamic range of the standards. Final concentrations are adjusted to account for dilution from original gel sample volume.

Fluorescence Lifetime Imaging (FLIM): Time-correlated single-photon counting (TCSPC) FLIM measurements were obtained using one of two custom MaiTai Ti:Sapph laser-scanning two-photon rigs with high-sensitivity PMT detectors. The first customized rig was used for early *in vitro* experiments and is detailed in the *in vitro* imaging section below; the second was custom made for *in vivo* experiments and is detailed in the *in vivo* imaging section below. In either case, ABP-dextran was excited at 760nm and emitted photons were subjected to a 445/58 bandpass filter prior to detection using high-sensitivity PMTs. Specific FLIM collection software differed between the two rigs and is detailed in the relevant sections below, but in either case a fluorescence lifetime is generated for each pixel by measuring the time it takes for an emitted photon to be detected, binning these photons according to arrival time, and to these data a first-order exponential equation is fit to derive the rate constant representing the fluorescence lifetime (Gehlen 2020). The presence of a quencher will shorten fluorescence lifetime to an extent which is linearly related to quencher concentration through the Stern-Volmer equation,

$$\frac{\tau_o}{\tau_i} = 1 + [Q]k_{SV}$$

where τ_o / τ_i represents the unquenched lifetime divided by the shortened lifetime at a given quencher concentration ([*Q*]; ibid). The Stern-Volmer constant (k_{SV}) of the resultant line relates the concentration of quencher to the shortening of fluorescence lifetime. Photons were collected over an acquisition period of 90seconds (*in vivo* and agarose gels) to 150seconds (*in vitro* slice cultures). Each individual pixel is fit to an exponential to yield a lifetime value, and summed to yield an intensity value. ABP-dextran k_{SV} used in calculations for a given experiment is derived from the specific batch of ABP-dextran calibrated on the specific microscope used and with settings used in the given experiment for which Cl^-_o is calculated. Image processing, calculations, and statistics were accomplished using custom routines developed in Matlab (v2018b; Mathworks, Natick, MA).

Calibration of ABP-dextran: We initially calibrated ABP-dextran against chloride in simple phosphate buffer (20mM; pH 7.2) with varying amounts of NaCl (0-150mM), such that solutions were essentially modified PBS. We also verified whether other biologically relevant anions were capable of quenching ABP using similar buffers with 20mM phosphate and 0-150mM anion, or

HEPES buffer (20mM; pH 7.2) when varying phosphate concentration. For subsequent experiments done in aCSF or in vivo, we calibrated ABP-dextran against aCSF with varying chloride concentrations. This was accomplished by preparing standard aCSF (in mM: NaCl 126; KCl 3.5; $CaCl_2$ 2; $MgCl_2$ 1.3; NaH_2PO4 1.2; Glucose 11; $NaHCO_3$ 15) and a low-chloride aCSF in which NaCl was replaced with sodium gluconate, having demonstrated gluconate had no appreciable effect on ABP-dextran quenching (Figure 1C). We mixed appropriate amounts of this low chloride aCSF with standard aCSF to achieve varying chloride concentrations (10-136mM) in which the sum of sodium chloride and sodium gluconate was kept constant at 136mM. FLIM calibrations were obtained for each batch of ABP-dextran on the same microscope and with the same range of laser powers used in experiments, though k_{SV} did not appreciably change between ABP-dextran batches or microscopes. Because calibrations done in aCSF have a minimum Cl^- of 10mM as described, the unquenched lifetime (τ_o) used for Stern-Volmer calculations is approximated as the y-intercept (Cl^- = 0mM) of a best-fit curve of the raw calibration data; empirically a biexponential fit was used (Figure 1B). All calculations are otherwise done as described under *Fluorescence Lifetime Imaging (FLIM)* section above. Notably, k_{SV} values did not differ appreciably between the aCSF and phosphate-buffered methods.

Animals: All animal protocols were approved by the Massachusetts General Hospital Institutional Animal Care and Use Committee. Wild type mice (C57bl/6; Jackson Labs 000664) of either sex were used for this study. Mouse pups remained in the home cage with the dam under standard husbandry conditions until postnatal day 6 to 8 (P6–8) when organotypic slice cultures were prepared or a cortical window was surgically placed.

In vitro organotypic slice cultures and imaging: Organotypic hippocampal slice cultures were prepared either as glass-mounted (Berdichevsky et al., 2016) or membrane insert-mounted (Stoppini et al., 1991) cultures. Briefly, in either case hippocampi are obtained from P6-8 mice and cut to 400μm thick slices. These are then gently transferred to a 6-well dish containing either a membrane insert (Millipore) or a poly-L-lysine coated coverslip (Electron Microscopy Sciences), are fed twice weekly with 1mL neurobasal-A media supplemented with 500μM Glutamax, 2% B-27, and 0.03mg/mL gentamycin (all from Invitrogen), and are incubated at 35C in a 5% CO_2 incubator. Cultures are typically imaged between DIV 12-21 in aCSF warmed to 33C and bubbled with 95:5::O_2:CO_2 perfused at a rate of approximately 100mL/hour unless otherwise noted. Slices were pretreated with 500μg/mL ABP-dextran for 1-2 hours prior to perfusing with aCSF containing 136mM chloride and the same concentration of ABP-dextran. Slices were allowed to equilibrate in perfusate for 20-30 minutes before imaging, equaling at least 2 hours of total exposure to ABP-dextran prior to initiation of imaging. Two photon images were captured with a 20x water-immersion objective, NA 0.90, on a customized Olympus BX50WI rig equipped with an 80MHz Ti:Sapphire MaiTai laser (SpectraPhysics) driven with customized software for microscope operation and Becker & Hickl SPC800 FLIM hardware and software for data collection and initial processing in FLIM mode. Photons must pass through a 445/58 bandpass emission filter before PMT detection (Hamamatsu C6438-01). Lifetime and intensity values for each pixel are generated using SPCImage software (Becker & Hickl) before being exported for use in custom Matlab processing routines.

In vivo murine cortical window imaging: Using a modified method based on that of Che et al. (Che and De Marco Garcia, 2021), we placed cortical windows in young adult mice (P26-34) for acute (non-survival) imaging in accordance with Massachusetts General Hospital Institutional

Animal Care and Use Committee policies and procedures (protocol 2018N000221). Full methods are included as a supplement. Briefly, anaesthetized mice were immobilized with standard ear bars and nosepiece until custom headbar is placed (Figure 5A). A section of scalp is removed to expose a roughly 1cm section of skull. Acrylic dental cement powder (Lang Dental, Wheeling IL) mixed with cyanoacrylate adhesive is used to fix the headbar to the exposed skull at 4 o'clock to Bregma, creating a 5mm diameter working area. A 2.5mm round section of skull and underlying dura is removed and a 3mm No. 1 coverslip is placed over the exposed cortex. Coverslip has 10μL concentrated ABP-dextran / agarose mixture (1%w/v low gelation temperature agarose with 10mg/mL ABP-dextran in aCSF) pipetted from 42C heat block immediately before inversion and placement. One hour is allowed before image acquisition for ABP-dextran diffusion into cortex from overlying agarose (between cortex and coverslip; Figure 5B) during which time the warmed breadboard with immobilization apparatus and anesthetized mouse is transferred to the *in vivo* imaging microscope, a custom-made gantry-type two-photon microscope equipped with a MaiTai 80MHz Ti:Sapphire laser (Spectraphysics) and driven with customized ScanImage software (MBF Bioscience, Williston, VT). Photons are detected by a high-sensitivity PMT (Hamamatsu C5594-12) after passing through a 445/58 bandpass emission filter (Chroma) and digitized using custom ScanImage software. All other components are from Thor Labs. The initial analysis of raw FLIM data generating fluorescence lifetime data for each pixel is accomplished using ImageJ plug-in FLIMJ. Subsequent analysis including region of interest selection, conversion to chloride values (see below), composite image generation and statistics are accomplished using custom routines in Matlab.

<u>Agarose or agar gel Cl^- determination using ABP-dextran FLIM:</u> Cl^- within an agar or agarose gel was measured using the two-photon rig described above in the "in vivo" section, except with a 4x (NA 0.28) objective. Using an 8-well microchamber with silicone dividing gasket (Ibidi, Grafelfing, Germany), gels were cast in aCSF containing ABP-dextran and subsequently transferred to a single Petri dish where they were equilibrated with aCSF containing ABP-dextran for at least 1 hour prior to imaging. FLIM measurements were taken as described, generally one field per quadrant at a depth of between 50-100microns. Importantly, the gasket separating gels of differing compositions was removed such that all gels in an experiment were bathed in the same aCSF with the same [Cl^-] (Figure 2C). Where gels were kept for more than 1 day, they were prepared in aCSF without glucose and kept refrigerated between readings to prevent fouling.

<u>Chondroitinase treatment of organotypic hippocampal slice cultures</u>: Chondroitinase ABC (ChABC; AMSBIO, #E1028-02) was brought up in aCSF containing 0.1% bovine serum albumin (BSA) to a concentration of 1U/mL. Slices grown on membrane inserts were treated for 1hour either with aCSF containing ChABC or sham aCSF containing only the 0.1% BSA vehicle. Both experiment and control had 0.5mg/mL ABP-dextran, and FLIM imaging was done using the two-photon rig described in the *in vivo* section above. At the conclusion of imaging, the aCSF was collected for detection of liberated chondroitin sulfate.

<u>Measurement of sulfated glycosamioglycans (sGAGs) liberated in aCSF</u>: Blyscan alcian blue-based kit (Biocolor, #B1000) was utilized for measurement of sGAGs including chondroitin sulfate proteoglycans (CSPGs). After treatment with aCSF containing ChABC or BSA vehicle as detailed above, aCSF was collected and measured as directed against standards of bovine trachea chondroitin (Blyscan kit standard) with appropriate amounts of 10x stocks of aCSF and

0.1% BSA to obtain concentrations identical to samples. Alcian blue reagent absorbance is read at 650nm.

Image processing in Matlab: ABP fluorescence lifetime is converted to Cl^-_o as described above. Regions of interest (ROIs) are defined using intensity images for organotypic hippocampal slice cultures as a differentiation between tissue and surrounding bath or between anatomically defined regions such as the stratum pyramidale, stratum radiatum and stratum oriens. ROIs are defined *in vivo* as cortical regions between anatomical landmarks, such as vessels, which are identified through their exclusion of ABP-dextran. ROIs are then converted to masks and applied to fluorescence lifetime data, which are then converted to Cl^-_o. Variance of cortical Cl^-_o is measured against ABP-dextran in aCSF calibration solutions. Each concentration of Cl^- in the calibration curve has a normally distributed set of ABP-dextran lifetime values with a near-constant relative standard deviation ($RSD = \frac{\sigma}{\mu}$). Fluorescence lifetime has a physical upper and lower bound over which its values are meaningful (lifetime in the absence of quencher vs fully quenched fluorophore). Specifically for ABP-dextran we have found lifetime values to be linearly related to Cl^- from 0mM - 150mM through the Stern-Volmer relationship. Using these bounds for image processing by excluding any pixels with lifetimes in excess of the mean at 0mM chloride or lifetimes shorter than twice the standard deviation less than the mean at 150mM (calculated from best-fit curve to raw calibration data and average RSD). Excluding all values outside this calibrated range represents an average exclusion of 0.5-1.5% of pixels obtained using Becker&Hickl FLIM and 0.1-0.5% of pixels using custom-built *in vivo* microscope. We then compared RSD values of ROIs to those of ABP-dextran in bulk solution to evaluate the extent of variation within differing regions. To assess the spatial distribution of local Cl^-_o, we modified methods recently developed to categorize intracellular chloride microdomains (Rahmati et al. 2021). Briefly, we binned Cl^-_o in a given field using uniform binwidths of < 1mM over the range of μ +/- 2σ. Neighboring pixels that were in the same bin and whose raw values were within one bin width were considered to be a domain of chloride at the mid-bin Cl^-_o. These domains were then further characterized as described using custom Matlab routines.

Results

Non-invasive measurement of extracellular chloride using ABP-dextran: ABP is a novel Cl-sensitive fluorophore compatible with **f**luorescence **l**ifetime **im**aging (FLIM) that we have optimized to be bright, red-shifted, and possessing a dynamic range that encompasses concentrations of chloride found in the extracellular space. We conjugated ABP to a 10,000 Dalton (10KDa) dextran resulting in an amine-bonded moiety resistant to pH changes in the physiological range that is restricted to the extracellular space (Figure 1A). We validated the ability of ABP-dextran to reliably report chloride concentration and calibrated the shortening of ABP-dextran fluorescence lifetime to chloride concentration (Figure 1B) which is linearly related through the Stern-Volmer relationship (Figure 1C) with a k_{SV} of 14.6 mM. The emission lifetime of ABP-dextran is not dependent upon the concentration of ABP-dextran, only the concentration of chloride. While chloride concentration also affects ABP-dextran intensity, as long as sufficient photons are collected to derive a single-exponential decay constant from a given pixel the concentration of chloride can be calculated (Figure 1D-G) independent of the actual ABP-dextran concentration.

Sulfated agarose gels as an in vitro model of perineuronal space: We recently observed that differing concentrations of chloride juxtaposed to one another were stable on time scales of at

least 100 minutes due to the presence of immobile anionic charge present in the intracellular space (Rahmati N et al., 2021). In order to explore whether this is possible in the extracellular space we modeled the interstitial matrix, the perineuronal lattice-like structures found around all neurons and first described by Golgi in 1898 (Golgi C, 1898; Celio MR et al., 1998), using gels of sulfated agarose to mimic the sulfated glycosaminoglycans such as the chondroitin sulfate-decorated aggrecan family members that are prominent in the perineuronal matrix. Agarose is a nominally sulfate-free glycopolymer that is a major component of Agar (Figure 2A; bars 1 and 2). We used agarose as a chemically homogenous starting material for covalent sulfate linkage. We optimized the method of Fuse and Suzuki (Fuse T and Suzuki T, 1975) to balance the retention of the gelation properties of agarose with high sulfate incorporation, because these properties are inversely related. We obtained a sulfated agarose which could be used to cast gels bearing 50mM effective sulfate concentration (Figure 2A; bar 3) covalently linked to the polymerized agarose lattice. Gels cast from sulfated agarose serve as a simple in vitro model of the perineuronal extracellular space, allowing us to investigate the ability of covalently linked anions attached to a three-dimensional matrix to displace mobile chloride ions. When we measured the chloride concentration within unsulfated agarose gels equilibrated in aCSF, we found no significant difference versus the perfusate aCSF (Figure 2B, left pair vs center pair) measured either with a standard colorimetric iron(III) thiocyanate assay (Figure 2B, black bars) or ABP-dextran FLIM imaging (Figure 2B, green bars). Agarose gels with fixed anions in the form of covalently bound sulfate had significantly decreased chloride concentrations versus control aCSF (Figure 2B, right vs center pair) or native agarose gels that had no fixed anions (Figure 2B, right vs left pair). Both assay methods, FLIM and iron thiocyanate, produced equivalent results (Figure 2B, black bar on left vs green bar on right of each pair). Next we placed separately cast unsulfated and sulfated gels adjacent to each other and equilibrated in the same aCSF bath with ABP-dextran. We were able to image both gels in the same field, along with aCSF filling a several micron gap between them, demonstrating that the presence of sulfate groups covalently bound to the polymerized gel results in a significantly decreased chloride concentration (Figure 2C; schematic inset). ABP-dextran FLIM measurements of chloride concentration within either unsulfated or sulfated gels demonstrated stable chloride concentration differences for over three weeks, consistent with the displacement of mobile chloride ions by the sulfates fixed to the gel (Figure 2D), a process commonly referred to as Donnan exclusion (Donnan 2011; Marinsky 1985; Helfferich 1995; Fatin-Rouge et al., 2003; Epsztein et al. 2018; Gao et al. 2022).

<u>Demonstration of chloride displacement in living systems:</u> Next we studied mouse hippocampal slice cultures to examine whether extracellular perineuronal fixed anions such as chondroitin sulfate-decorated aggrecan family proteoglycans displace chloride in a living system. After pretreatment with ABP-dextran and equilibration with aCSF containing ABP-dextran and 136mM chloride, we measured extracellular chloride concentration using ABP-dextran FLIM and found an unexpectedly low and heterogenous Cl^-_o. A representative field is shown in Figure 3A. Perineuronal traces along the outer circumference of neuronal silhouettes (white dashes) were used to analyze the pixel-wise change in Cl^-_o in the extracellular space immediately adjacent to the neuronal cytoplasmic membrane (Figure 3A-C). We compared the size of the effects of fixed anions on local Cl^-_o to Brownian and machine noise arising from FLIM of ABP-dextran in bulk solutions with similar mean Cl^-_o (red plots in Figure 3B and D; red dashes in 3C). The pixel-to-pixel change in Cl^-_o (ΔCl^-_o) versus distance in the presence of fixed anions in the perineuronal space (Figure 3B, blue) was much larger than the ΔCl^-_o versus distance in the absence of fixed

anions in bulk solution containing the same concentration of Cl and ABP-dextran (Figure 3B, red). Collecting data from a larger cohort of perineuronal tracings of varying lengths and their corresponding aCSF solution counterparts and plotting the observed variability in chloride concentration (expressed as ΔCl^-_o per micron) in the presence or absence of fixed anions we found a consistently increased probability of greater ΔCl^-_o where fixed extracellular anions were present (Figure 3D, blue vs red), including a notable three-fold increase in ΔCl^-_o versus distance at the 50% and 90% probability points. We then confirmed that fixed anions, including chondroitin sulfate-decorated glycoproteins, are at least partially responsible for this difference by measuring Cl^-_o before and after treatment with chondroitinase. Analogous to matrix metalloprotease activation, chondroitinase is a bacterial enzyme that cleaves the sulfated glycopolymer chondroitin. We demonstrate that organotypic slice cultures treated with chondroitinase have significantly increased Cl^-_o (Figure 4A&B; pre- and post-digestion, respectively) and that this approximately 10mM increase in freely diffusible chloride within the slice culture (Figure 4C&D; light blue digested vs dark blue [pre] or black [sham] controls) coincides with a significant decrease of extracellular fixed anions within the slice culture as measured by an increase of released polysulfated chondroitin in the perfusate after digestion (Figure 4E). These observations are consistent with the proposed inverse relationship of fixed extracellular anions and mobile Cl^-_o, as loss of chondroitin sulfate after digestion with chondroitinase (Figure 4E) coincides with an observed increase in Cl^-_o (Figure 4A&B; quantified in 4C; analyzed statistically in 4D).

<u>Chloride displacement in the perineuronal space in vivo:</u> To test whether Donnan exclusion of Cl^-_o by sulfated GAGs was significant *in vivo*, we performed live 2 photon imaging of P26-34 mice via a cortical window. Direct application of high concentrations of ABP-dextran within the agar overlying the neocortex (Figure 5B) resulted in a robust ABP fluorescence signal from both the extracellular space of the brain parenchyma and the agarose above the cortex, with notable exclusion of fluorescence emission from blood vessels (Figure 5C) and cell bodies (Figure 5C inset). Expanded regions of interest from a representative cortical image (Figure 5C&D) are plotted in Figure 5D together with the signal from the overlying column of agar brought up in aCSF with 136mM chloride. All 82 regions of interest studied across 19 fields and 5 animals had Cl^-_o that was less than half the chloride concentration measured in the agar column, which was set to a standard rodent aCSF value of 136 mM (e.g. Weilinger et al, 2022). Regional mean Cl^-_o values were approximately 50-60mM (Figure 5E) but there was notable spatial variation between regions and even within regions (Figure 5F), consistent with local Donnan exclusion by variably sulfated GAGs. Regions with homogenous chloride concentrations have dimensions in the micron range, i.e. extracellular chloride microdomains. The lower limit of the size of such domains was below the resolution of our 2 photon system (0.5micron; Figure 5F). There was no characteristic values of Cl^-_o associated with these extracellular microdomains (Figure 5F). Thus the chloride concentration is much lower than expected in the extracellular space of the neocortex and is spatially heterogenous, creating Cl^-_o microdomains.

1. <u>Discussion</u>

Summary of results: We demonstrate stable Donnan exclusion of chloride by fixed anions in sulfated agar using both FLIM of a novel fluorophore, ABP-dextran, as well as chemical assays of sulfate and chloride. FLIM of ABP-dextran demonstrated that Cl^-_o in the brain is less than half the Cl concentration in the cerebrospinal fluid and plasma. This low Cl^-_o arises from Donnan exclusion of chloride by fixed sulfated glycosaminoglycans, because release of sGAGs by

chondroitinases results in an increase in Cl^-_o that corresponds to the amount of sulfates released. The distribution of chloride in the extracellular space of the brain varies substantially at micrometer dimensions, creating extracellular chloride microdomains.

Limitations of this study

The finding that Cl^-_o is much lower than expected in the extracellular space of living brain tissue is based on FLIM of a new Cl-sensitive fluorophore, ABP-dextran. These results are in contrast to the higher values measured using ion sensitive electrodes (Jiang et al. 1992; Kroeger et al. 2010). The ABP-dextran fluorophore is based on a validated structure (Biwersi et al. 1992) and was calibrated against Cl, other anions, and direct chemical analysis chloride concentrations in situ. ABP-dextran FLIM accurately reported Cl values in sulfated carbohydrate polymers (Figure 2), so it is unlikely that the sGAGs or other anions in the extracellular environment affected the accuracy of the ABP-dextran FLIM. ABP-dextran overcomes several barriers to accurate measurement of extracellular chloride, including sufficient sensitivity in the relevant range of chloride concentrations, competition with autofluorescence, and permeation into the cytoplasmic space, where lower chloride values would be encountered. ABP-dextran was clearly excluded from the intracellular space (Figure 3A; Figure 5C inset) and was far brighter than autofluorescence at 760nm 2-photon excitation. We speculate that the difference between the fluorophore-based measures and the ion-sensitive electrode measures of Cl^-_o likely arise from distortion of the extracellular milieu created by the stab wound of the microelectrode such that the microelectrode measures chloride in fluid comprised of bulk CSF rather than fluid in which Donnan exclusion is operative.

Stable Donnan exclusion

An important finding in this study is that Cl microdomains established by Donnan exclusion are stable for weeks, and do not require active transport to be maintained (Figure 2). This phenomenon is well-established in biophysics (e.g. Epsztein et al. 2018; Gao et al. 2022), but is more confusing in neuronal physiology where membranes with time-varying ionic permeabilities and transporters create a more complex environment (Voipio et al. 2014; Dusterwald et al. 2018; Doyon et al. 2016; Rahmati et al. 2021). A point of particular confusion is the role of active Cl transport vs. Donnan exclusion in maintaining a particular E_{GABA} in the face of GABA-gated Cl flux that alters the local Cl concentration. After a GABA-gated Cl influx, and re-establishment of local charge balance by cationic flux via voltage- and ligand-gated cation channels, the local cytoplasm will contain excess chloride salts. This Cl has two fates: either excess salt diffuses through the cytoplasm to re-establish a new equilibrium with fixed anionic charges, or the excess salt is transported back across the membrane by cation-chloride cotransporters (Brumback et al. 2008; Lewin et al. 2012; Doyon et al. 2016; Beckstein and Naughton 2022). The transporters are required to re-establish the original steady state volume, but in the absence of transport, diffusion maintains local Cl concentrations remarkably well (Brumback et al. 2008; Rahmati et al. 2021). In the absence of membrane Cl salt transport, this diffusion of excess Cl salts will be associated with either a cytoplasmic volume increase from associated water influx or an increase in the mean Cl concentration in the cytoplasm. At pathologically high rates of Cl influx, membrane chloride salt transport becomes rate-limiting (Staley et al. 1999; Jedlicka et al. 2011; Lewin et al. 2012; Doyon et al. 2016), and chloride concentrations become sufficiently labile to depolarize E_{GABA} (e.g. Barker and Ransom 1978; Alger and Nicoll 1982; Huguenard and Alger 1986, Staley et al. 1995). Thus Donnan exclusion *establishes* the local value of E_{GABA}, and active transport *maintains* that value (and neuronal

volume) in the face of synaptic Cl flux (Glykys et al. 2014). The same principals should apply to the local extracellular chloride concentrations described here, with astrocytic chloride buffering taking the place of neuronal membrane cation-chloride cotransport (Egawa et al. 2012)

Low extracellular Cl

The Cl^-_o measured by ABP FLIM is less than half of the canonical Cl^-_o. Such a low value of Cl^-_o should affect not only E_{GABA} but also the inhibitory $GABA_A$ conductance, because there are only half as many ions to carry the outward membrane currents (i.e. inward Cl- flux; Coombs et al. 1955). Shouldn't such a low value of Cl^-_o have been obvious from electrophysiological studies? E_{GABA} is determined by the ratio of Cl^-_I to Cl^-_o (ibid; Staley 2022). If either concentration is known, the other can be determined from E_{GABA}. However If both Cl^-_i and Cl^-_o are determined by the concentrations of local immobile anions, neither can be set experimentally, so E_{GABA} cannot be used to determine either Cl^-_i or Cl^-_o; only the ratio can be determined. Similarly, although the conductance of inward Cl flux (outward membrane current) is determined in part by $Cl^-_{o,}$ it is also determined by the $GABA_A$ permeability, i.e. the number of open membrane channels and their capacity for ion flux. Thus membrane currents are not sufficient to determine Cl^-_o (Coombs et al. 1955). Control of the ionic milieu is greater in single-channel recordings, but whether the complement of immobile anions is physiological under these conditions is difficult to determine, and even in these conditions there is substantial uncertainty regarding local ionic concentrations (Li et al. 2016).

Cl^-_o microdomains

The extracellular matrix of the brain is often depicted as perineural nets surrounding parvalbumin neurons that are detected by specific agglutinins and antibodies (Celio and Blumke 1994). However, these assays detect very specific motifs of glycosaminoglycan sulfation; using more permissive methods, a highly anionic extracellular matrix can be seen to surround virtually all neurons (Golgi 1898; Glykys et al. 2014; Morawski et al. 2015). This extracellular matrix fills the extracellular space, which comprises about 20% of the brain's volume (Sykova and Nicholson 2008; Tonneson et al. 2018). The sGAG moieity of proteoglycans are the primary constituent of extracellular matrix (Frantz et al. 2010; Karamanos et al. 2021). GAGs are polymers of widely varied length comprised of sugars and substituted sugars (N-acetylglucosamine, glucuronic acid, and galactose) that are synthesized without templates. Up to 3 sulfates are added to the sugar moieties before export to the extracellular space. This enables the creation of a highly variant spatial distribution of fixed anionic charge in the extracellular matrix. Figure 3 demonstrates that this variance is substantial at the level of resolution of light microscopy. However, the distribution of fixed anions at the extracellular face of $GABA_A$ receptors, and the corresponding Cl^-_o, is currently unknown.

Physiological implications

Cl^-_o microdomains in the region of the extracellular openings of $GABA_A$ receptor-operated channels are a critical determinant of both E_{GABA} and the $GABA_A$ conductance. The wide range of Cl^-_o values established via Donnan exclusion by sulfated GAGs (Figures 2, 3, 4 and 5) makes possible a substantial variety of effects of $GABA_A$ receptor activation based on the direction of chloride flux. These effects range from hyperpolarizing inhibition through shunting inhibition through excitation by activation of low threshold calcium currents and removal of the magnesium block of the NMDA receptor. In addition, the effects of Cl^-_o on the quantity of charge that is carried by $GABA_A$ membrane currents (the conductance; Coombs et al. 1955) makes

possible a broad range of strengths of $GABA_A$ synapses that is independent of the number or subunit composition of receptors or their phosphorylation status.

The turnover of the macromolecules comprising the extracellular matrix is very slow (Tsien 2013), on the order of months to years based on rodent experiments (Margolis and Margolis 1973) and the rate of deterioration of patients with genetic defects of GAG catabolism (Heron et al. 2011; Seo et al. 2020; Hampe et al. 2020). This slow turnover provides a mechanism for long-lasting influences on synaptic GABA signaling. Some elements of GAG synthesis are activity dependent (Sidharthan et al. 2013), but currently nothing is known about the insertion of GAGs into the extracellular matrix, in situ modification, and the capacity for directed alterations of Cl^-_o microdomains in the regions of $GABA_A$ receptors and synapses. Thus the role of extracellular chloride microdomains in synaptic signal processing and memory remain to be discovered.

Pathological implications

Cytotoxic cerebral edema: If Cl^-_o is normally only half of the value of Cl in CSF and plasma, then the capacity for Cl^-_o to increase acutely may be an important and hitherto unappreciated element of the pathophysiology of cerebral edema (Glykys et al. 2017). Matrix metalloproteinases (MMPs) are released and activated after neuronal injury and death (Zhang et al. 2016). Release of sulfates in sGAGs from the extracellular matrix would reduce the Donnan exclusion of Cl by fixed sulfates. This would result in an acute increase of Cl^-_o as in Figure 4. The action of equilibritave cation-Cl cotransporters would then lead to a corresponding increase in chloride salts in the cytoplasm of neighboring healthy neurons, with attendant volume increases. This novel mechanism of cytotoxic edema could potentially be ameliorated by pharmacological MMP inhibition. Alternatively, inhibition of the influx of chloride salts that cross the BBB from the vascular space (Jha et al., 2019) would limit the influx of Cl into the extra and intracellular spaces.

Post Traumatic Epilepsy: Richard Miles and colleagues demonstrated that $GABA_A$ receptor activation could be excitatory in human brain tissue resected for control of medically intractable epilepsy (Cohen et al. 2002). However, the pathomechanism has never been elucidated (Huberfeld et al. 2007; Karlocai et al. 2015; Gonzalez 2016). Gliosis is the most common finding in medically intractable epilepsy (Thom 2014). In glial scars, reactive astrocytes replace the extracellular matrix (Roll and Faissner 2013; Song and Dityatev 2018). If the replacement matrix was more heavily sulfated than the original, as would be expected from the firm texture that is responsible for the name “scar” (Lesperance et al. 1992), then in areas of gliosis Cl^-_o would be low. Low Cl^-_o could result in degradation of $GABA_A$ receptor mediated inhibition, frank excitation, and failure of anticonvulsants whose action are predicated on intact synaptic inhibition. Thus replacement of the extracellular matrix and distortion of extracellular chloride microdmains could comprise an important mechanism of medically intractable epilepsy after brain injury.

Future studies

The findings that Cl^-_o is both lower than expected and spatially heterogenous opens the door for many investigations into the mechanisms by which Cl^-_o is set, such as the synthesis, export, and in situ modification of sGAGs. The activity dependence of these mechanisms and the effect of Cl^-_o microdomains on synaptic signaling are additional areas of investigation. Pathologically, the

impact of changes in Cl^-_o in both acute edema and long-term complications such as epilepsy may provide much-needed therapeutic insights into these frequently-intractable conditions.

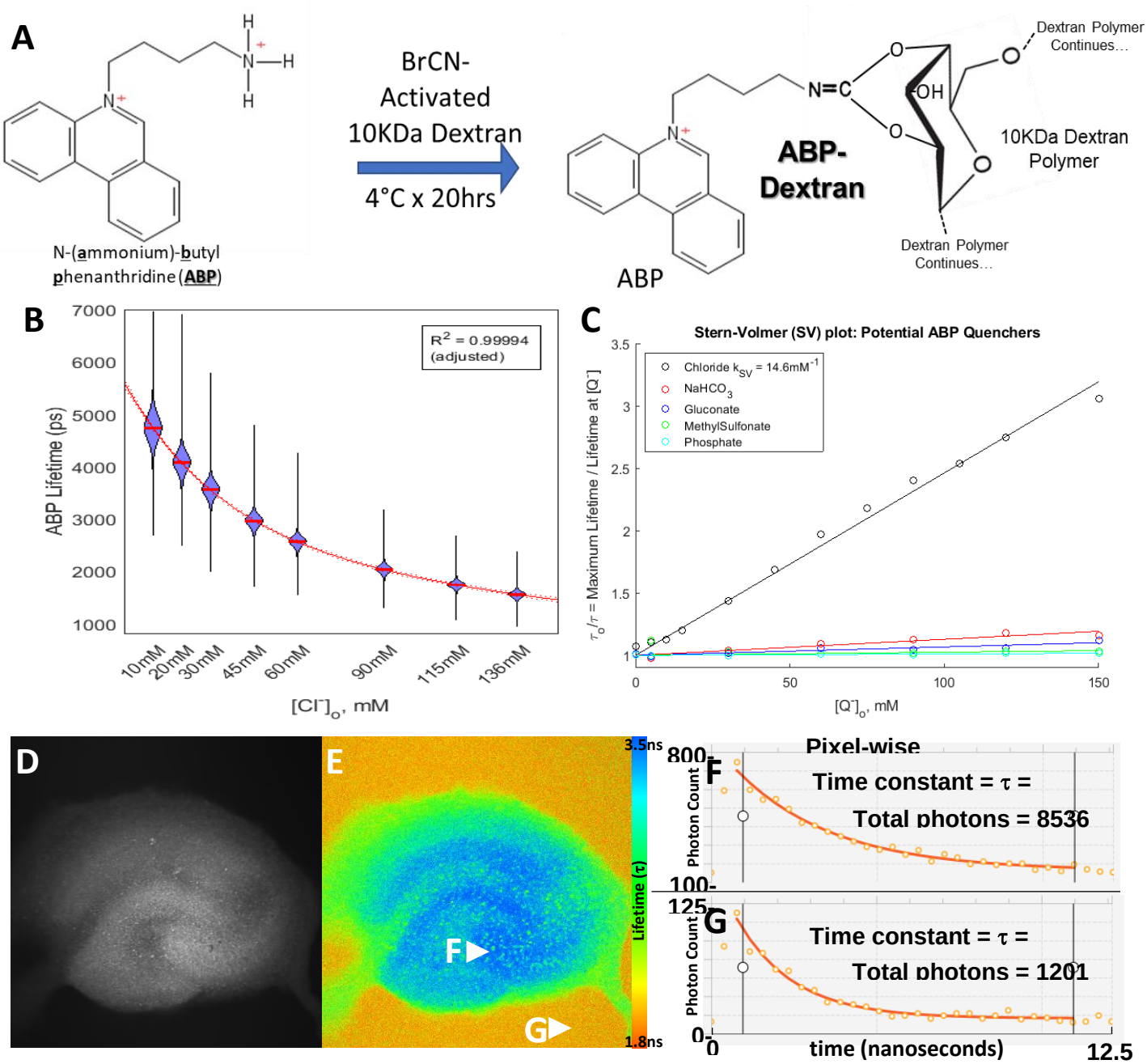

Figure 1 Characterization and Calibration of Chloride-Sensitive Fluorophore ABP. ***A)*** N-(ammonium)-butyl phenanthridine (ABP) is synthesized in-house and conjugated to activated dextran, a glucose polymer, at a ratio of 10-14 fluorescent molecules per 10KDa Dextran. ***B)*** Chloride quenching both attenuates the intensity and shortens the fluorescence lifetime of ABP-dextran. Unlike intensity, fluorescence lifetime signal is independent of the concentration of fluorophore thus we rely on fluorescence lifetime imaging (FLIM) of ABP. ***C)*** Fluorescence lifetime is linearly related to quencher concentration through the Stern-Volmer relationship, and chloride calibration is presented (black). Other biological anions were confirmed inactive with respect to ABP quenching. ***D&E)*** Total intensity image (***D***) equal to the total photons collected in each pixel between 80MHz laser pulses, a period of 12.5 nanoseconds (ns) which is divided into 32 bins of 0.391ns each and used to fit a single exponential curve whose decay constant is

equal to fluorescence lifetime (tau; τ) shown in ***E*** with locations of pixels detailed in ***F*** and ***G*** indicated with white arrowheads. Pseudocolor in ***E*** shows longer lifetimes with cooler colors (lower Cl^-_o) and shorter lifetimes are warmer colors (higher Cl^-_o). ***F&G)*** Single exponential fit demonstrations from individual pixels representing a high-intensity area (***F***; CA3) and a low-intensity area (***G***; aCSF perfusate) highlighting that despite a seven-fold difference in photons collected there is sufficient signal in both pixels to calculate the fluorescence lifetime, tau (τ), from which $[Cl^-]$ is subsequently calculated as described.

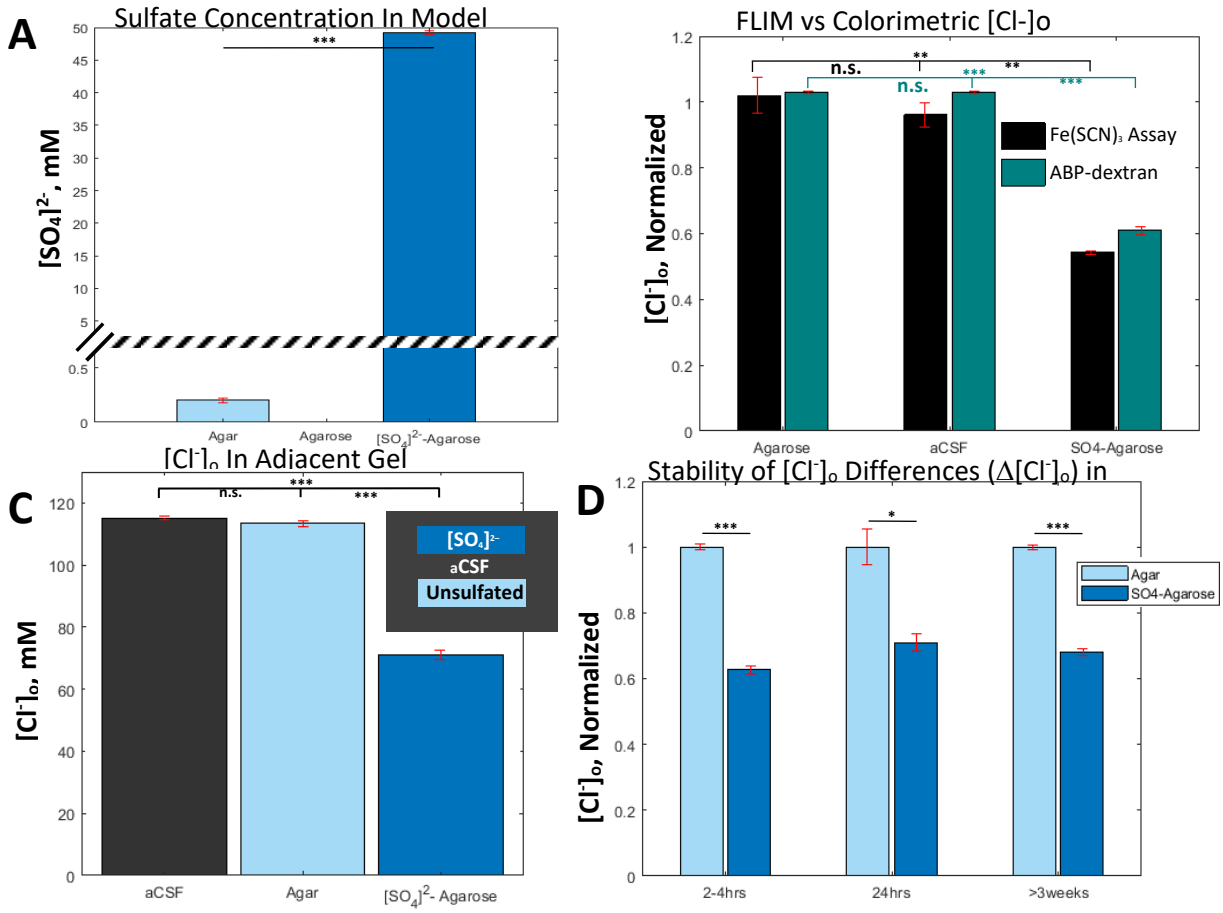

<u>Figure 2:</u> Effects of immobile sulfate on Cl^- in a volume of agarose gel. ***A)*** We sulfated algal biopolymer agarose and cast this as a gel in aCSF to model perineuronal interstitial matrix that is rich in chondroitin sulfate-decorated glycosaminoglycans. We compared sulfated agarose gel to native agar and agarose gels, achieving a 250-fold increase in sulfate content compared to commercially available agar (bar 3 vs bar 1; note broken y-axis); commercially available agarose (bar 2) had no measurable sulfate content. ***B)*** Direct comparison of chloride concentrations in native agarose gel (leftmost pair) or sulfated agarose gel (rightmost pair) cast in aCSF versus agarose-free bulk aCSF control (center pair), measured using either colorimetric chemical assay (black bars, left) or ABP-dextran FLIM (green bars, right) demonstrating a significant inverse relationship between chloride concentration and fixed anionic charge using either method. ***C)*** Demonstration of stable juxtaposition of significantly different chloride concentrations. Experimental schematic (inset, upper right) indicates spatial relationship of separately cast gel pieces placed abutting one another and equilibrating in the same aCSF; under magnification an aCSF-filled gap between them is visible. Measured chloride concentrations in sulfated agarose (dark blue) or unsulfated agar (light blue) demonstrate that areas of significantly lower chloride can and do stably exist where fixed anionic charges are covalently incorporated into the three-dimensional matrix as compared with native agarose (bars 2 vs 3) or bulk aCSF (charcoal; bars 1 vs 3). ***D)*** These significant chloride differences are stable for as long as experimentally observed—greater than three weeks. *Statistical significance (*) as determined using Student's paired t-test at $p < 0.05$ level; ** indicates $p <$*

*0.005, *** indicates p < 0.0005; “n.s.” is non-significant .*

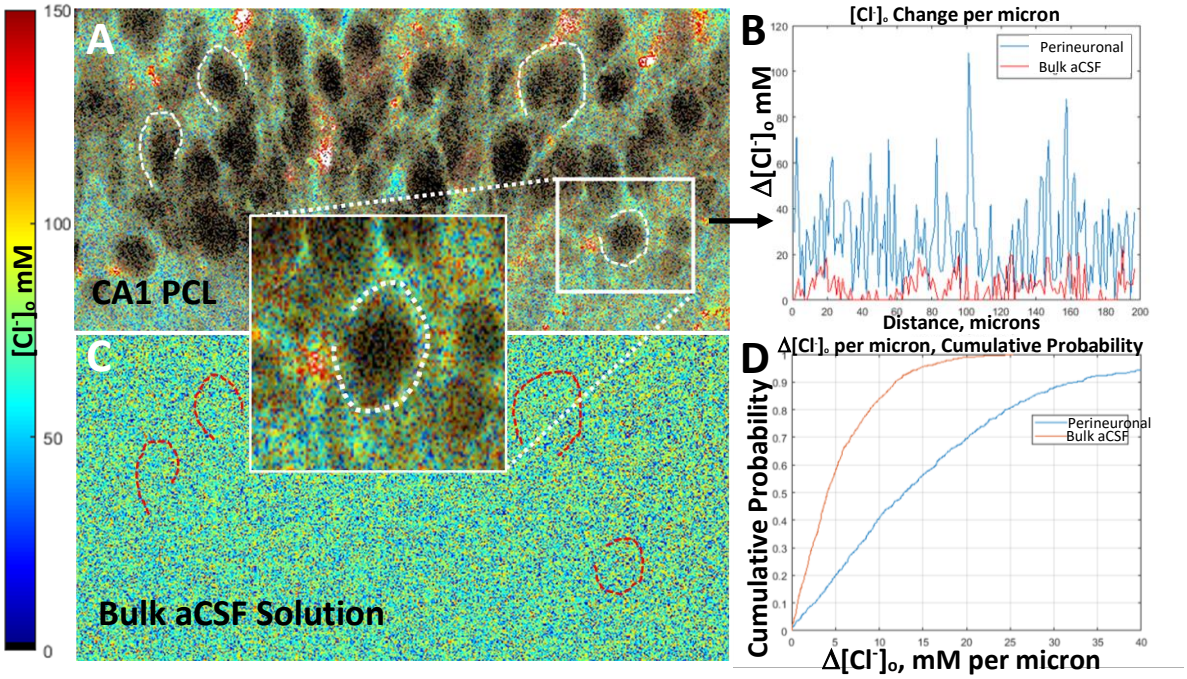

<u>Figure 3</u> Cl^-_o displacement by Perineuronal Fixed Anions in organotypic hippocampal slice cultures. ***A)*** ABP-dextran, perfused in aCSF containing 136mM chloride, is excluded from neurons in mouse organotypic hippocampus slice cultures as demonstrated by somatic silhouettes (CA1 pyramidal cell layer [PCL]); neurons are identified by morphology. Tracing of perineuronal space (white dashes) is shown for several neurons and the change in chloride concentration (ΔCl^-_o) versus distance of one representative neuron is plotted in ***B*** (blue line; zoomed inset). ***B)*** Comparison of Δ Cl^-_o versus distance around the perineuronal space of the cell indicated in ***A*** (white box; zoomed inset) and the same trace laid over bulk aCSF (red line) as a measure of variance due to Brownian and machine noise, indicated in ***C*** by red dashes. ***C)*** Bulk aCSF solution analyzed as a stochastic control. The same traces from CA1 pyramidal cell layer (PCL; ***A***) are applied to bulk aCSF solution (red dashes) laid over the same part of an identically acquired field, providing the "Bulk aCSF" data in ***B&D***. Variance in ***C*** is indicative of stochastic Brownian and machine noise and can be compared qualitatively to the zoomed area of the slice culture (zoomed inset across ***A&C***) and quantitatively in ***B&D*** (red vs blue). ***D)*** Quantification of variance attributable to extracellular fixed anions for several perineuronal traces (blue line) or their bulk aCSF solution controls (red line) expressed as the cumulative probability of the observed change in Δ Cl^-_o per micron distance around eight pyramidal cells in two representative slices analyzed as in ***B***.

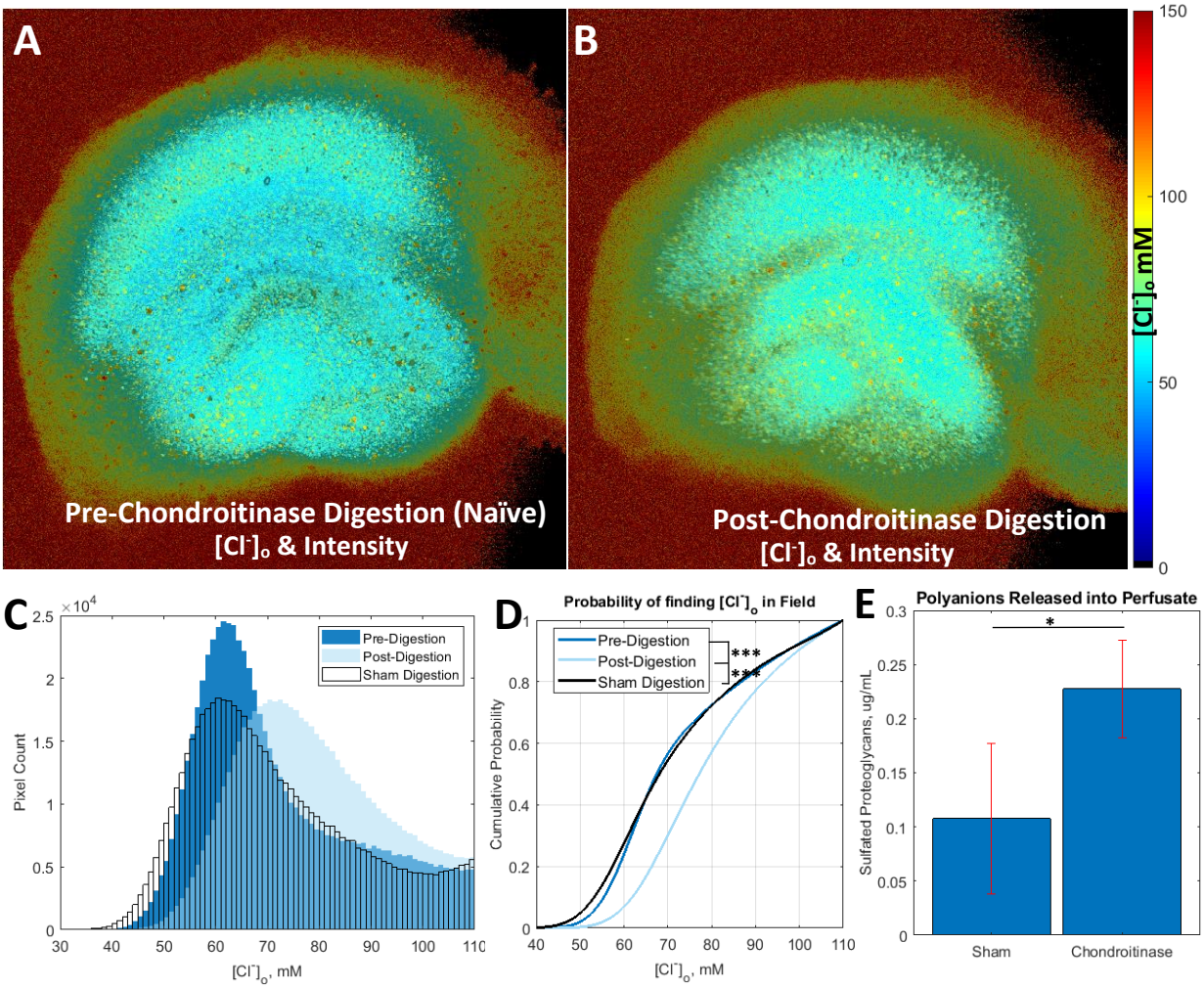

<u>Figure 4:</u> Cl^-_o displacement attenuated after removal of fixed perineuronal anions by chondroitinase treatment. ***A&B)*** Composite images of representative mouse hippocampus slice culture perfused in aCSF containing 136mM chloride and 500ug/mL ABP-dextran before (***A***) and after (***B***) treatment with bacterial MMP analog chondroitinase. Colormap corresponds to [Cl-]o, calculated from fluorescence lifetime of ABP-dextran, while ABP-dextran intensity data provides structure-defining contrast (see ***Figure1 D&E*** for examples of raw lifetime and intensity images). Bulk aCSF surrounding the slice contains 136mM chloride and provides a second peak centered at this value which is not shown in ***C&D***. ***C)*** Histogram of Cl^-_o corresponding to pre-digestion naïve slice culture with unaltered fixed perineuronal anions (dark blue; image in ***A***) and the same slice after treatment with chondroitinase (light blue; image in ***B***) along with sham digestion slice treated with chondroitinase vehicle (unfilled black outline; slice image not shown). Pixels not meeting statistical fit requirements (Chi squared < 1) are excluded from ***C&D*** (corresponding pixels in ***A&B*** are black). ***D)*** Cumulative probability function of Cl^-_o in interstitial matrix, i.e. perineuronal extracellular space, for the leftmost peak corresponding to hippocampal slice cultures. Cl^-_o in the interstitial matrix after chodroitinase treatment is significantly higher

than either before treatment (light blue vs dark blue) or after sham treatment (light blue vs black), consistent with a decreased presence of fixed anions. ***E)*** Measurement of polysulfated chondroitin (polyanions) released into the perfusate after treatment with chondroitinase (vs sham) using a commercial colorimetric assay demonstrates that a significantly higher concentration of polyanions are found in the extracellular fluid after chondroitinase digestion, consistent with the release of chondroitin sulfate from extracellular matrix within slice cultures and a resultant increase in Cl^-_o. *All slice cultures were DIV14-21 at time of experiment; * indicates statistical significance at $p < 0.05$ by paired t-test (**E**; $p = 0.017$); *** indicates statistical significance at $p < 0.0001$ by Kolmogorov-Smirnov paired-sample test (**D**).*

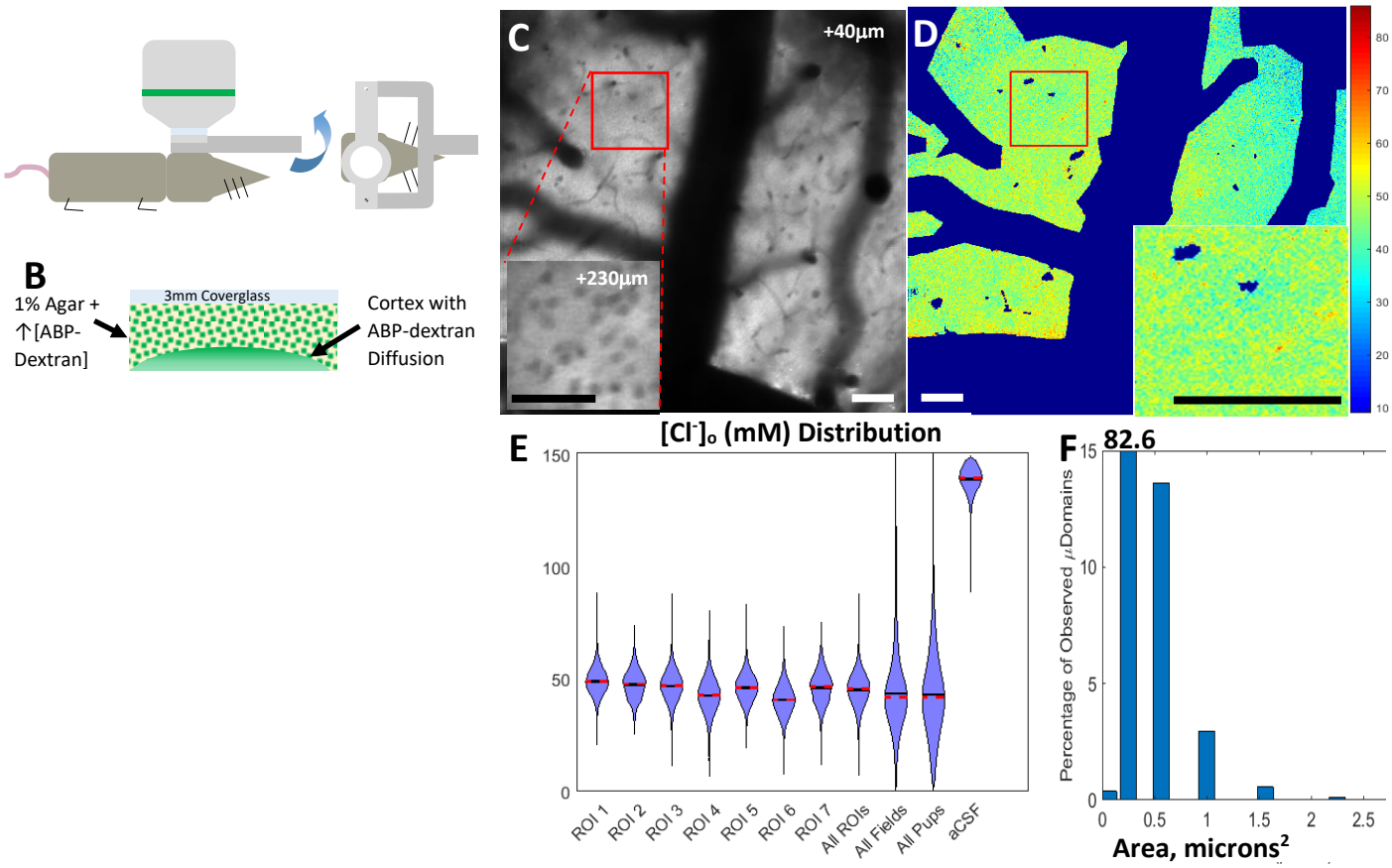

<u>Figure 5</u> Cl^-_o in murine cortex is less than half that of CSF. *A&B)* Schematic in vivo cortical window experimental setup, demonstrating immobilization strategy, window placement, and ABP-dextran diffusion from agar/aCSF into cortical extracellular space. ***C)*** ABP-dextran intensity at a depth of 40microns (µm) demonstrating vasculature silhouettes in layer 1 cortex; inset shows plane 190µm further from cortical surface (230µm) demonstrating cellular silhouettes in layer 2/3 cortex. ***D)*** $[Cl^-]_o$ calculated from ABP-dextran fluorescence lifetime, demonstrating the ROIs selected in this field. Rectangle (red; upper left) indicates the area enlarged 5x in inset, revealing areas of similar Cl^-_o (bin size <1mM) within a variegated field. ***E)*** Violin plots detailing Cl^-_o distributions in each region of interest (ROI) in ***D***, all 7 ROIs collectively, all 8 fields from this animal, all 5 mouse pups in this data set, and ACSF value measured within the agar placed between exposed cortex and the cortical window. ***F)*** Distribution of multiple-pixel areas of Cl^-_o, with a sizeable minority at least one half square micron. *All scale bars indicate 20*mm*; Cl^-_o colorbar scaled to whole field mean +/- 2*sigma and filled with 64 colors (see methods).*

Supplemental Methods:

Sulfation of Agarose: The goal of maximizing sulfation must be balanced with the consequent erosion of gel properties such as gelation and water holding capacity. Agarose was added to a well-dried Erlenmeyer flask and dissolved in DMSO at a concentration of 4%(w/v) at room temperature before being cooled to 4C with stirring. Addition of 4:1 mixture of acetic anhydride / glacial acetic acid, also pre-chilled to 4C, was added to agarose/DMSO mixture (2 parts to 5 parts). Vigorous mixing by hand was necessary to thin the gelatinous mixture to a slurry and allow stirring at 4C for 15 minutes; gentle heat transfer from experimenter's hands likely helped loosen the initial gel but care is taken to return the mixture to 4C. Concentrated sulfuric acid is then added slowly at specified molar ratio to repeating disaccharide unit, D-galactose – 3,6-anhydro-L-galactopyranose, at 4C with stirring. Diluted sulfuric acid should be avoided, as the presence of water under acidic conditions promotes hydrolysis of the polymer and diminishes gelation. Mixture is then allowed to stir at ambient temperature for an additional 15 minutes. The reaction is then stopped by neutralization with 10M NaOH, again with stirring at 4C. This is also an exothermic process; mixture is chilled in an ice bath prior to and periodically during neutralization. Ideal temperature is 10-15C and is not allowed to exceed room temperature. 10M NaOH neutralization unavoidably adds water to the acidic mixture, which promotes hydrolysis of the polymer and must be done with as much haste as tolerable while keeping the temperature of the solution in the specified range. Once 90% of the calculated base necessary to neutralize the solution has been added, pH is monitored with a 3-point calibrated pH meter (insert specifics) until a weakly basic pH is achieved (7.20). Sulfated agarose is then dialyzed in 12-14KDa dialysis tubing (SpectraPor, S432703) against 15 volumes of 50mM Tris pH 7.4 for 2-3 hours, then distilled water changed twice daily until dialysate clarifies. Agarose is then precipitated by adding 200-proof ethanol to achieve 95% ethanol/water and cooling to 4C at least 4hours. Vacuum filtered material was subsequently dried in 50C oven as an alternative to lyophilization. Material is stored at ambient temperature in sealed glass vial until use.

<u>Fluorescence Lifetime Imaging (FLIM)</u>: Time-correlated single-photon counting (TCSPC) FLIM measurements were obtained using one of two custom MaiTai Ti:Sapph laser-scanning two-photon rigs with high-sensitivity PMT detectors. The first customized rig was used for early in vitro experiments and is detailed in the in vitro imaging section below; the second was custom made for in vivo experiments and is detailed in the in vivo imaging section below. In either case, ABP-dextran was excited at 760nm and emitted photons were subjected to a 445/58 bandpass filter prior to detection using high-sensitivity PMTs. Specific FLIM collection software differed between the two set-ups and is detailed in the relevant sections below, but in either case each pixel had an associated histogram expressing photon number vs photon travel time (the delay between excitation and detection) which was fitted to a single exponential curve to derive a time constant *k*,

$$(1)\ A_t = A_o e^{-kt}$$

denoting the fluorescence lifetime of the fluorophore derived from each pixel. As implied by Equation 1, fluorescence lifetime is an intrinsic property of the fluorophore and wholly independent of fluorophore concentration. However, fluorescence lifetime may be shortened (i.e., quenched) by one or more moieties in a manner dependent upon the concentration of the quencher – *not the concentration of the fluorophore itself*. In the case of the fluorophore used in the present study (ABP), chloride is the lone biologically relevant quencher. The degree of

lifetime shortening relative to the initial unquenched lifetime is linearly related to the concentration of the quencher through the Stern-Volmer relationship,

$$(2)\ \frac{\tau_o}{\tau_i} = 1 + [Q]k_{SV}$$

where τ_o / τ_i represents the unquenched lifetime divided by the shortened lifetime at a given quencher concentration ([Q]), necessarily yielding a y-intercept of 1 (Gehlen, 2020). The slope of the resultant plot, referred to as the Stern-Volmer constant (k_{SV}), facilitates conversion of measured fluorescence lifetime to concentration of quencher. Notably, there is no term to describe fluorophore concentration in Equation 2 as the fluorophore concentration has no impact on measured lifetime. Only the concentration of the quencher, chloride, affects the fluorescence lifetime. Images are acquired over 1.5 minutes (*in vivo* and agarose gels) to 2.5 minutes (*in vitro* slice cultures), with each pixel having a histogram of photons populating time bins from which a single exponential time constant (fluorescence lifetime) and intensity value (summed photons from all bins) are derived. Utilizing the k_{SV} derived from the specific batch of ABP-dextran used in a given experiment and calibrated on the same microscope used under experimental conditions and settings, Cl^-_o is calculated in living tissue or in agarose gels from lifetime values (calibration described in detail below). These calculations, as well as intensity-based region of interest selection and subsequent processing, is accomplished using custom routines developed in Matlab (v2018b, using signal processing and statistics toolboxes).

Bibliography

Alger BE, Nicoll RA. Pharmacological evidence for two kinds of GABA receptor on rat hippocampal pyramidal cells studied in vitro. J Physiol. 1982 Jul;328:125-41.

Barker JL, Ransom BR. Amino acid pharmacology of mammalian central neurones grown in tissue culture. J Physiol. 1978 Jul;280:331-54.

Beckstein O, Naughton F. General principles of secondary active transporter function. Biophys Rev (Melville). 2022 Mar;3(1):011307. doi: 10.1063/5.0047967. Epub 2022 Mar 29. PMID: 35434715; PMCID: PMC8984959.

Berdichevsky Y, Saponjain Y, Park KI, Roach B, Pouliot W, Lu K, Swiercz W, Dudek FE, Staley KJ. Staged anticonvulsant screening for chronic epilepsy. Ann Clin Transl Neurol 2016 Oct 18;3(12):908-923. Doi: 10.1002/acn3.364. PMID: 28097203, PMCID: PMC5224819.

Biwersi J, Farah N, Wang YX, Ketcham R, Verkman AS. Synthesis of cell-impermeable Cl-sensitive fluorescent indicators with improved sensitivity and optical properties. Am J Physiol. 1992 Jan;262(1):C242-50. doi: 10.1152/ajpcell.1992.262.1.C243. PMID: 1370743.

Brumback AC, Staley KJ. Thermodynamic regulation of NKCC1-mediated Cl- cotransport underlies plasticity of GABA(A) signaling in neonatal neurons. J Neurosci. 2008 Feb 6;28(6):1301-12. doi:

Celio MR, Blümcke I. Perineuronal nets--a specialized form of extracellular matrix in the adult nervous system. Brain Res Brain Res Rev. 1994 Jan;19(1):128-45. doi: 10.1016/0165-0173(94)90006-x. PMID: 8167657.

Celio MR, Spreafico R, De Biasi S, Vitellaro-Zuccarello L. Perineuronal nets: past and present. *Trends Neurosci*. 1998 Dec;21(12):510-5. doi: 10.1016/s0166-2236(98)01298-3. PMID: 9881847.

Chahine NO, Chen FH, Hung CT, Ateshian GA. Direct measurement of osmotic pressure of glycosaminoglycan solutions by membrane osmometry at room temperature. Biophys J. 2005 Sep;89(3):1543-50. doi: 10.1529/biophysj.104.057315. Epub 2005 Jun 24. PMID: 15980166; PMCID: PMC1366659.

Che A and De Marco Garcia NV. An in vivo calcium imaging approach fro the identification of cell-type specific patterns in the developing cortex. Front Neural Circuits 2021 Oct 5;15:747724. Doi: 10.3389/fncir.2021.747724. PMID: 34690708, PMCID: PMC8528153.

Cohen I, Navarro V, Clemenceau S, Baulac M, Miles R. On the origin of interictal activity in human temporal lobe epilepsy in vitro. Science. 2002 Nov 15;298(5597):1418-21

Coombs JS, Eccles JC, Fatt P. The specific ionic conductances and the ionic movements across the motoneuronal membrane that produce the inhibitory post-synaptic potential. J Physiol. 1955 Nov 28;130(2):326-74. doi: 10.1113/jphysiol.1955.sp005412. PMID: 13278905; PMCID: PMC1363415.

DiRaddo JO, Miller EJ, Bowman-Dalley C, Wroblewska B, Javidnia M, Grajkowska E, Wolfe BB, Liotta DC, Wroblewski JT. Chloride is an Agonist of Group II and III Metabotropic Glutamate Receptors. Mol Pharmacol. 2015 Sep;88(3):450-9. doi: 10.1124/mol.114.096420. Epub 2015 Jun 18. PMID: 26089372.

Donnan FG. Theory of membrane equilibria and membrane potentials in the presence of nondialysing electrolytes: a contribution to physical-chemical physiology. Translation published in the Journal of Membrane Science 100 (1995) 45-55; originally published in Zeitschrift fur Elektrochemie und angewandte physikalische Chemie, 17 (1911) 572-581.

Doyon, N., Vinay, L., Prescott, S. A., and De Koninck, Y. (2016). Chloride regulation: a dynamic equilibrium crucial for synaptic inhibition. Neuron 89, 1157-1172

Düsterwald KM, Currin CB, Burman RJ, Akerman CJ, Kay AR, Raimondo JV. Biophysical models reveal the relative importance of transporter proteins and impermeant anions in chloride homeostasis. Elife. 2018 Sep 27;7. pii: e39575.

Ebihara S, Shirato K, Harata N, Akaike N. Gramicidin-perforated patch recording: GABA response in mammalian neurones with intact intracellular chloride. J Physiol. 1995 Apr 1;484 (Pt 1)(Pt 1):77-86. doi: 10.1113/jphysiol.1995.sp020649. PMID: 7541464; PMCID: PMC1157923.

Egawa K, Yamada J, Furukawa T, Yanagawa Y, Fukuda A. Cl^- homeodynamics in gap junction-coupled astrocytic networks on activation of GABAergic synapses. J Physiol. 2013 Aug 15;591(16):3901-17. doi: 10.1113/jphysiol.2013.257162. Epub 2013 Jun 3. PMID: 23732644; PMCID: PMC3764636.

Epsztein R, Shaulsky E, Dizge N, Warsinger DM, Elimelech M. Role of Ionic Charge Density in Donnan Exclusion of Monovalent Anions by Nanofiltration. Environ Sci Technol. 2018 Apr 3;52(7):4108-4116. doi: 10.1021/acs.est.7b06400. Epub 2018 Mar 14. PMID: 29510032.

Fatin-Rouge N, Milon A, Buffle J, Goulet RR, Tessier A (2003) Diffusion and partitioning of solutes in agarose hydrogels: the relative influence of electrostatic and specific interactions. J Phys Chem B 107:12126–12137. doi: 10.1021/jp0303164

Florence TM, Farrar YJ. Spectrophotometric determination of chloride at the parts-per-billion level by the mercury(II) thiocyanate method. Anal. Chim. Acta, 54(1871) 373-377, 1971

Frantz C, Stewart KM, Weaver VM. The extracellular matrix at a glance. Journal of Cell Science. 2010;123(24):4195-200.

Fuse T and Suzuki T. Preparation and properties of agar sulfates. Agric Biol Chem, 39:119 (1975). doi: 10.1080/00021369.1975.10861571

Gao KW, Yu X, Darling RM, Newman J, Balsara NP. Increased Donnan exclusion in charged polymer networks at high salt concentrations. Soft Matter. 2022 Jan 5;18(2):282-292. doi: 10.1039/d1sm01511g. PMID: 34918729.

Gehlen, MH. The centenary of the Stern-Volmer equation of fluorescence quenching: from the single line plot to the SV quenching map. J Photochem Photobiol C: Photochem Rev. v42 March 2020. doi: 10.1016/j.jphotochemrev.2019.100338.

Golgi C *Boll. Soc. Med-chir. Pavia* 1, 1–14, 1898; *Rend. Ist. Lomb. Sci. Lett*. 31, 1–12, 1898.

González MI. Regulation of the cell surface expression of chloride transporters during epileptogenesis. Neuroscience Letters 628 (2016) 213–218

Grimley JS, Li L, Wang W, Wen L, Beese LS, Hellinga HW, Augustine GJ. Visualization of synaptic inhibition with an optogenetic sensor developed by cell-free protein engineering automation. J Neurosci. 2013 Oct 9;33(41):16297-309. doi: 10.1523/JNEUROSCI.4616-11.2013. PMID: 24107961; PMCID: PMC3792465.

Hampe CS, Eisengart JB, Lund TC, Orchard PJ, Swietlicka M, Wesley J, McIvor RS. Mucopolysaccharidosis Type I: A Review of the Natural History and Molecular Pathology. Cells. 2020 Aug 5;9(8):1838.

Helfferich FG (1995) Ion exchange. New York: Dover. 3rd edition.

Héron B, Mikaeloff Y, Froissart R, Caridade G, Maire I, Caillaud C, Levade T, Chabrol B, Feillet F, Ogier H, Valayannopoulos V, Michelakakis H, Zafeiriou D, Lavery L, Wraith E, Danos O, Heard JM, Tardieu M. Incidence and natural history of mucopolysaccharidosis type III in France and comparison with United Kingdom and Greece. Am J Med Genet A. 2011 Jan;155A(1):58-68.

Hu H, Gan J, Jonas P. Interneurons. Fast-spiking, parvalbumin^{+} GABAergic interneurons: from cellular design to microcircuit function. Science. 2014 Aug 1;345(6196):1255263. doi: 10.1126/science.1255263. Epub 2014 Jul 31. PMID: 25082707.

Huberfeld G, Wittner L, Clemenceau S, Baulac M, Kaila K, Miles R, Rivera C. Perturbed chloride homeostasis and GABAergic signaling in human temporal lobe epilepsy. J Neurosci. 2007 Sep 12;27(37):9866-73.

Huguenard JR, Alger BE. Whole-cell voltage-clamp study of the fading of GABA-activated currents in acutely dissociated hippocampal neurons. J Neurophysiol. 1986 Jul;56(1):1-18.

Jedlicka P, Deller T, Gutkin BS, Backus KH. Activity-dependent intracellular chloride accumulation and diffusion controls GABA(A) receptor-mediated synaptic transmission. Hippocampus. 2011 Aug;21(8):885-98.

Jha RM, Kochanek PM, Simard JM. Pathophysiology and treatment of cerebral edema in traumatic brain injury. Neuropharmacology. 2019 Feb;145(Pt B):230-246. doi: 10.1016/j.neuropharm.2018.08.004. Epub 2018 Aug 4. PMID: 30086289; PMCID: PMC6309515.

Jiang C, Agulian S, Haddad GG. Cl- and Na+ homeostasis during anoxia in rat hypoglossal neurons: intracellular and extracellular in vitro studies. J Physiol. 1992 Mar;448:697-708. doi: 10.1113/jphysiol.1992.sp019065. PMID: 1593484; PMCID: PMC1176223.

Kaneko H, Putzier I, Frings S, Kaupp UB, Gensch T. Chloride accumulation in mammalian olfactory sensory neurons. J Neurosci. 2004 Sep 8;24(36):7931-8. doi: 10.1523/JNEUROSCI.2115-04.2004. PMID: 15356206; PMCID: PMC6729923.

Karamanos NK, Theocharis AD, Piperigkou Z, Manou D, Passi A, Skandalis SS, Vynios DH, Orian-Rousseau V, Ricard-Blum S, Schmelzer CEH, Duca L, Durbeej M, Afratis NA,

Troeberg L, Franchi M, Masola V, Onisto M. A guide to the composition and functions of the extracellular matrix. The FEBS journal. 2021;288(24):6850-912.

Karlocai MR, Wittner L, Toth K, Maglo´czky Z, Katarova Z, Ra´sonyi G, Eross R, Czirja S, Hala´sz P Szabo G, Payne JA, Kaila K, Freund T. Enhanced expression of potassium-chloride cotransporter KCC2 in human temporal lobe epilepsy. Brain Struct Funct (2016) 221:3601–3615

Kroeger D, Tamburri A, Amzica F, Sík A. Activity-dependent layer-specific changes in the extracellular chloride concentration and chloride driving force in the rat hippocampus. J Neurophysiol. 2010 Apr;103(4):1905-14. doi: 10.1152/jn.00497.2009. Epub 2010 Feb 3. PMID: 20130043.

Kuner T, Augustine GJ. A genetically encoded ratiometric indicator for chloride: capturing chloride transients in cultured hippocampal neurons. Neuron. 2000 Sep;27(3):447-59. doi: 10.1016/s0896-6273(00)00056-8. PMID: 11055428.

Lesperance LM, Gray ML, Burstein D. Determination of fixed charge density in cartilage using nuclear magnetic resonance. J Orthop Res. 1992 Jan;10(1):1-13. doi: 10.1002/jor.1100100102. PMID: 1309384.

Lewin N, Aksay E, Clancy CE. Computational modeling reveals dendritic origins of GABA(A)-mediated excitation in CA1 pyramidal neurons. PLoS One. 2012;7(10):e47250. doi: 10.1371/journal.pone.0047250. Erratum in: PLoS One. 2013;8(5). doi: 10.1371/annotation/d6af29ee-25c0-4f8e-910e-afe53ef8f963. PMID: 23071770; PMCID: PMC3470566.

Li M, Toombes GE, Silberberg SD, Swartz KJ. Physical basis of apparent pore dilation of ATP-activated P2X receptor channels. Nat Neurosci. 2015 Nov;18(11):1577-83. doi: 10.1038/nn.4120. Epub 2015 Sep 21. PMID: 26389841; PMCID: PMC5113834.

Margolis RK, Margolis RU. The turnover of hexosamine and sialic acid in glycoproteins and mucopolysaccharides of brain. Biochim Biophys Acta. 1973 Apr 28;304(2):413-20.

Marinsky JA (1985) An interpretation of the sensitivity of weakly acidic (basic) polyelectrolyte (cross-linked and linear) equilibria to excess neutral salt. J Phys Chem 89:5294–5302.

Morawski M, Reinert T, Meyer-Klaucke W, Wagner FE, Tröger W, Reinert A, Jäger C, Brückner G, Arendt T. Ion exchanger in the brain: Quantitative analysis of perineuronally fixed anionic binding sites suggests diffusion barriers with ion sorting properties. Sci Rep. 2015 Dec 1;5:16471. doi: 10.1038/srep16471. PMID: 26621052; PMCID: PMC4664884.

Plested AJ, Mayer ML. Structure and mechanism of kainate receptor modulation by anions. Neuron. 2007 Mar 15;53(6):829-41. doi: 10.1016/j.neuron.2007.02.025. PMID: 17359918.

Rahmati N, Kunzelmann K, Xu J, Barone S, Sirianant L, De Zeeuw CI, Soleimani M. Slc26a11 is prominently expressed in the brain and functions as a chloride channel: expression in Purkinje cells and stimulation of V H^+-ATPase. Pflugers Arch. 2013 Nov;465(11):1583-97. doi: 10.1007/s00424-013-1300-6. Epub 2013 Jun 4. PMID: 23733100.

Rahmati N, Normoyle KP, Glykys J, Dzhala VI, Lillis KP, Kahle KT, Raiyyani R, Jacob T, Staley KJ. Unique actions of GABA arising from cytoplasmic chloride microdomains. J Neurosci. 2021 June9;41(23):4957-4975. doi: 10.1523/JNEUROSCI.3175-20.2021. PMID:33903223, PMCID: PMC8197632.

Roll L, Faissner A. Influence of the extracellular matrix on endogenous and transplanted stem cells after brain damage. Front Cell Neurosci. 2014 Aug 19;8:219.

Seo JH, Okuyama T, Shapiro E, Fukuhara Y, Kosuga M. Natural history of cognitive development in neuronopathic mucopolysaccharidosis type II (Hunter syndrome): Contribution of genotype to cognitive developmental course. Mol Genet Metab Rep. 2020 Jul 29;24:100630.

Sidharthan NP, Minchin RF, Butcher NJ. Cytosolic sulfotransferase 1A3 is induced by dopamine and protects neuronal cells from dopamine toxicity: role of D1 receptor-N-methyl-D-aspartate receptor coupling. J Biol Chem. 2013 Nov 29;288(48):34364-74

Song I, Dityatev A. Crosstalk between glia, extracellular matrix and neurons. Brain Res Bull. 2018 Jan;136:101-108.

Staley KJ, Mody I. Shunting of excitatory input to dentate gyrus granule cells by a depolarizing GABAA receptor-mediated postsynaptic conductance. J Neurophysiol. 1992 Jul;68(1):197-212. doi: 10.1152/jn.1992.68.1.197. PMID: 1381418.

Staley K "Ionic mechanisms of ictogenic disinhibition" in Jasper's Basic Mechanisms of the Epilepsies 2022 in press.

Stoppini L, Buchs PA and Muller D. A simple method for organotypic cultures of nervous tissue. J Neurosci Methods 1991 Apr;37(2):173-82. Doi: 10.1016/0165-0270(91)90128-m. PMID: 1715499.

Sulis Sato S, Artoni P, Landi S, Cozzolino O, Parra R, Pracucci E, Trovato F, Szczurkowska J, Luin S, Arosio D, Beltram F, Cancedda L, Kaila K, Ratto GM. Simultaneous two-photon imaging of intracellular chloride concentration and pH in mouse pyramidal neurons in vivo. Proc Natl Acad Sci U S A. 2017 Oct 10;114(41):E8770-E8779. doi: 10.1073/pnas.1702861114. Epub 2017 Sep 26. PMID: 28973889; PMCID: PMC5642681.

Sykova E, Nicholson C. Diffusion in Brain Extracellular Space. Physiological reviews. 2008;88(4):1277-340.

Thom M. Review: Hippocampal sclerosis in epilepsy: a neuropathology review. Neuropathol Appl Neurobiol. 2014 Aug;40(5):520-43

Thompson SM, Deisz RA, Prince DA. Relative contributions of passive equilibrium and active transport to the distribution of chloride in mammalian cortical neurons. J Neurophysiol. 1988 Jul;60(1):105-24. doi: 10.1152/jn.1988.60.1.105. PMID: 3404212.

Titze J, Shakibaei M, Schafflhuber M, Schulze-Tanzil G, Porst M, Schwind KH, Dietsch P, Hilgers KF. Glycosaminoglycan polymerization may enable osmotically inactive Na+ storage in the skin. Am J Physiol Heart Circ Physiol. 2004 Jul;287(1):H203-8. doi:

10.1152/ajpheart.01237.2003. Epub 2004 Feb 19. Erratum in: Am J Physiol Heart Circ Physiol. 2004 Sep;287(3):H1433. PMID: 14975935.

Tønnesen J, Inavalli VVGK, Nägerl UV. Super-Resolution Imaging of the Extracellular Space in Living Brain Tissue. Cell. 2018 Feb 22;172(5):1108-1121.e15. doi: 10.1016/j.cell.2018.02.007. PMID: 29474910.

Tora AS, Rovira X, Cao AM, Cabayé A, Olofsson L, Malhaire F, Scholler P, Baik H, Van Eeckhaut A, Smolders I, Rondard P, Margeat E, Acher F, Pin JP, Goudet C. Chloride ions stabilize the glutamate-induced active state of the metabotropic glutamate receptor 3. Neuropharmacology. 2018 Sep 15;140:275-286. doi: 10.1016/j.neuropharm.2018.08.011. Epub 2018 Aug 11. PMID: 30102917.

Torres PB, Nagai A, Jara CEP, Santos JP, Chow F, Cursino dos Santos DYA. Determination of sulfate in algal polysaccharide samples: a step-by-step protocol using a microplate reader. Ocean and Coastal Research, 2021 v69:e21021. doi: 10.1590/2675-2824069.21-010pbt.

Tremblay R, Lee S, Rudy B. GABAergic Interneurons in the Neocortex: From Cellular Properties to Circuits. Neuron. 2016 Jul 20;91(2):260-92. doi: 10.1016/j.neuron.2016.06.033. PMID: 27477017; PMCID: PMC4980915.

Tsien RY. Very long-term memories may be stored in the pattern of holes in the perineuronal net. Proc Natl Acad Sci U S A. 2013 Jul 23;110(30):12456-61.

Tyzio R, Minlebaev M, Rheims S, Ivanov A, Jorquera I, Holmes GL, Zilberter Y, Ben-Ari Y, Khazipov R. Postnatal changes in somatic gamma-aminobutyric acid signalling in the rat hippocampus. Eur J Neurosci. 2008 May;27(10):2515-28. doi: 10.1111/j.1460-9568.2008.06234.x. PMID: 18547241.

Verkman S. Development and biological applications of chloride-sensitive fluorescent indicators. Am J Physiol. 1990 Sep;259(3 Pt 1):C375-88. doi: 10.1152/ajpcell.1990.259.3.C375. PMID: 2205105.

Voipio J, Boron WF, Jones SW, Hopfer U, Payne JA, Kaila K. Comment on "Local impermeant anions establish the neuronal chloride concentration". Science. 2014 Sep 5;345(6201):1130. doi: 10.1126/science.1252978.

Urban JP, Maroudas A, Bayliss MT, Dillon J. Swelling pressures of proteoglycans at the concentrations found in cartilaginous tissues. Biorheology. 1979;16(6):447-64. doi: 10.3233/bir-1979-16609. PMID: 534768.

Weilinger NL, Wicki-Stordeur LE, Groten CJ, LeDue JM, Kahle KT, MacVicar BA. KCC2 drives chloride microdomain formation in dendritic blebbing. Cell Rep. 2002 Oct25;(41)4:111556. Doi: 10.1016/j.celrep.2022.111556. PMID: 36288701

Xiao F, Nicholson C, Hrabe J, Hrabetová S. Diffusion of flexible random-coil dextran polymers measured in anisotropic brain extracellular space by integrative optical imaging. Biophys J. 2008 Aug;95(3):1382-92. doi: 10.1529/biophysj.107.124743. Epub 2008 May 2. PMID: 18456831; PMCID: PMC2479597.

Zhang YW, Uchendu S, Leone V, Bradshaw RT, Sangwa N, Forrest LR, Rudnick G. Chloride-dependent conformational changes in the GlyT1 glycine transporter. Proc Natl Acad Sci U S A. 2021 Mar 9;118(10):e2017431118. doi: 10.1073/pnas.2017431118. PMID: 33658361; PMCID: PMC7958241.

Zhang S, Kojic L, Tsang M, Grewal P, Liu J, Namjoshi D, Wellington CL, Tetzlaff W, Cynader MS, Jia W. Distinct roles for metalloproteinases during traumatic brain injury. Neurochem Int. 2016 Jun;96:46-55.